

Atomically dispersed chromium coordinated with hydroxyl clusters enabling efficient hydrogen oxidation on ruthenium

Received: 28 May 2022

Accepted: 27 September 2022

Published online: 06 October 2022

Check for updates

Bingxing Zhang¹, Baohua Zhang¹, Guoqiang Zhao¹, Jianmei Wang¹, Danqing Liu¹, Yaping Chen¹, Lixue Xia², Mingxia Gao¹, Yongfeng Liu¹ , Wenping Sun¹ & Hongge Pan^{1,3}

Overcoming the sluggish kinetics of alkaline hydrogen oxidation reaction (HOR) is challenging but is of critical importance for practical anion exchange membrane fuel cells. Herein, abundant and efficient interfacial active sites are created on ruthenium (Ru) nanoparticles by anchoring atomically isolated chromium coordinated with hydroxyl clusters ($\text{Cr}_1(\text{OH})_x$) for accelerated alkaline HOR. This catalyst system delivers 50-fold enhanced HOR activity with excellent durability and CO anti-poisoning ability via switching the active sites from Ru surface to $\text{Cr}_1(\text{OH})_x$ -Ru interface. Fundamentally different from the conventional mechanism merely focusing on surface metal sites, the isolated $\text{Cr}_1(\text{OH})_x$ could provide unique oxygen species for accelerating hydrogen or CO spillover from Ru to $\text{Cr}_1(\text{OH})_x$. Furthermore, the original oxygen species from $\text{Cr}_1(\text{OH})_x$ are confirmed to participate in hydrogen oxidation and H_2O formation. The incorporation of such atomically isolated metal hydroxide clusters in heterostructured catalysts opens up new opportunities for rationally designing advanced electrocatalysts for HOR and other complex electrochemical reactions. This work also highlights the importance of size effect of co-catalysts, which should also be paid substantial attention to in the catalysis field.

Anion exchange membrane fuel cells (AEMFCs) possess the promising application foreground over proton-exchange membrane fuel cells (PEMFCs) as nonprecious metal electrocatalysts can be substituted for the platinum-group-metal (PGM)-based electrocatalysts in the cathodic oxygen reduction reaction^{1–3}. However, the anodic hydrogen oxidation reaction (HOR) of AEMFCs still relies on PGM-based catalysts for achieving desirable performance. The much more sluggish HOR kinetics in alkaline media further makes AEMFCs require higher loading of PGM-based catalysts to achieve the ideal power density compared to PEMFCs^{4–7}. In this respect, ever-increasing effort has recently

been devoted to developing active alkaline HOR electrocatalysts, particularly non-PGM-based catalysts, and to uncovering the intrinsic reasons for the inferior HOR activity in alkaline media^{8–13}. Despite considerable progresses have been achieved, breakthrough in terms of developing robust alkaline HOR electrocatalysts and in-depth understanding of the alkaline HOR mechanism is still urgent at this stage.

Electrocatalysts with an optimized surface/interface or electronic structure will largely balance the adsorption of intermediates (e.g., H, OH, and CO), thus enhancing their hydrogen electrocatalysis and anti-poisoning performance^{14–16}. In this regard, various approaches

¹School of Materials Science and Engineering, State Key Laboratory of Clean Energy Utilization, Zhejiang University, Hangzhou 310027, PR China. ²State Key Laboratory of Silicate Materials for Architectures, International School of Materials Science and Engineering, Wuhan University of Technology, Wuhan 430070, PR China. ³Institute of Science and Technology for New Energy, Xi'an Technological University, Xi'an 710021, PR China.

e-mail: wenpingsun@zju.edu.cn; honggepan@zju.edu.cn

such as doping or alloying^{17–24} and heterostructure engineering^{25–31} have been widely proposed to enhance the activity and durability of HOR electrocatalysts. However, most of these strategies can only partially resolve the problems of alkaline HOR. For example, the nanoscale heterostructure engineering focuses on the bifunctional mechanism²⁵, which merely optimizes the OH binding energy (OHBE) with the help of the transition metal (hydr)oxides but fails to tune the H binding energy (HBE), and hence provides very limited interfacial active sites. Although the alloying method can regulate the HBE by altering the electronic structure and provide abundant active sites^{17,23}, the doped metallic atom possesses less oxophilicity for OH⁻ adsorption as compared with its oxide counterpart²³. Therefore, it is highly important to develop an efficient strategy to simultaneously optimizing HBE and OHBE with groundbreaking insights for innovating HOR pathway.

In this work, combining the structural features of single-atom alloy and heterostructure catalysts, we design a distinctive Ru-based catalyst anchored by atomically dispersed chromium coordinated with hydroxyl clusters (Ru–Cr₁(OH)_x) for accelerated HOR kinetics (Fig. 1). Particularly, the isolated Cr₁(OH)_x clusters, as the co-catalyst, can maximize interfacial active sites and create abundant active oxygen species for optimizing HBE and promoting hydrogen or CO spillover from Ru to Cr₁(OH)_x. Based on the isotope-labeling experiments, the original oxygen species from Cr₁(OH)_x are also confirmed to react with adsorbed hydrogen for a faster hydrogen oxidation kinetics. As results, the HOR activity of Ru–Cr₁(OH)_x is 50-fold higher than the unmodified Ru. In addition, the isolated Cr₁(OH)_x clusters are also conducive to removing the CO molecules and suppressing the aggregation of Ru species during HOR, eventually delivering excellent CO-tolerance and long-durability performance. The proposed strategy is superior to typical designs of (hydr)oxide nano-modifiers and alloy catalyst, also presents fundamentally different HOR mechanism compared with conventional insights centered on surface metal sites.

Results and discussion

Material synthesis and characterization

The Ru–Cr₁(OH)_x catalyst was synthesized by a sequential reduction and deposition method followed by freeze drying (See Methods),

during which the metallic Ru nanoparticles were rapidly formed and concomitantly anchored by the Cr₁(OH)_x clusters (Supplementary Fig. 1). High-angle annular dark-field scanning transmission electron microscopy (HAADF-STEM), scanning electron microscopy (SEM) and transmission electron microscopy (TEM) images (Fig. 2a, Supplementary Figs. 2 and 3) of the Ru–Cr₁(OH)_x catalyst show an interconnected network structure with an aerogel morphology and average particle size of 2.4 nm. The X-ray diffraction (XRD) pattern (Supplementary Fig. 4) shows that Ru–Cr₁(OH)_x presents the sole metallic Ru structure and no Cr-based crystalline phase can be detected. High-resolution HAADF-STEM images (Fig. 2b, c) show the presence of a less electron-dense layer on the surface of metallic Ru nanoparticles, which is composed of the atomically dispersed Cr species with low weight loading on Ru surface. The interplanar distances of 0.21 nm is assigned to the (002) planes of Ru (Fig. 1b). Energy-dispersive X-ray spectroscopy (EDS, EDS, Supplementary Fig. 5) elemental mapping and electron energy loss spectroscopy (EELS, Fig. 1d) mapping images show the Cr, Ru and O species are homogeneously dispersed in both entire catalysts and one single nanoparticle. It can also be observed that the distributions of Cr and O species are very consistent and more obvious than that of Ru signal on the edge of nanoparticle (Fig. 2d). Furthermore, the signals of Cr and O species are not beyond the scope of Ru nanoparticle, suggesting it stays as the oxygen coordinated Cr₁ species on Ru surface but not a multiple-atom overlapped shell, which is further confirmed by the isolated Cr signal in the selected local EELS mapping image (Supplementary Fig. 6). For the chemical state of Cr, the obvious Cr (III) signal in EELS collected on the edge of Ru particle (Fig. 2e, f) confirms it is trivalent Cr₁ species anchored on Ru surface. The EDS line-scanning profile (Fig. 2g) also clearly evidences the Ru surface is covered with Cr and O species. Inductively coupled plasma-optical emission spectroscopy (ICP-OES, Supplementary Table 1) demonstrates the amount of Cr in Ru–Cr₁(OH)_x is 1.1 wt% (denoted as Ru–Cr₁(OH)_{x-1.1}). Time-of-flight secondary ion mass spectrometry (ToF-SIMS) spectra were further performed and reveal that single Cr (III) ion peaks are observed while other Cr–O multimers cannot be obviously detected, again confirming the atomically dispersed Cr (III) species on Ru nanoparticles³² (Supplementary Fig. 7). The above results together confirm the atomically dispersed Cr (III) coordinated

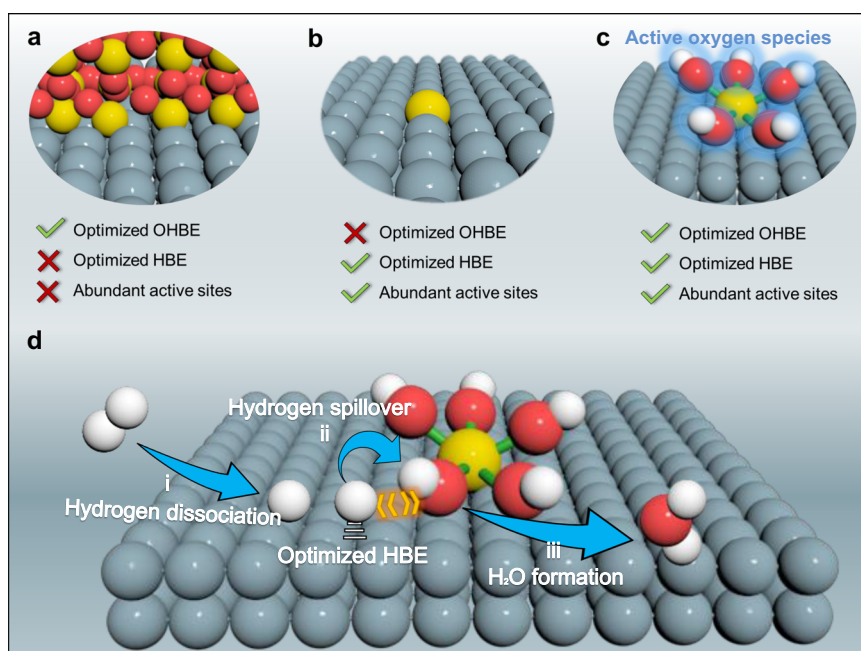


Fig. 1 | Scheme illustration of the proposed catalyst design strategy for HOR. Typically reported heterostructure (a) and single-atom alloy (b) catalysts for HOR. c The structure of Ru–Cr₁(OH)_x catalyst. d Proposed HOR mechanism for Ru–Cr₁(OH)_x catalyst. Color: Gray, Ru; yellow, Cr; red, O; white, H.

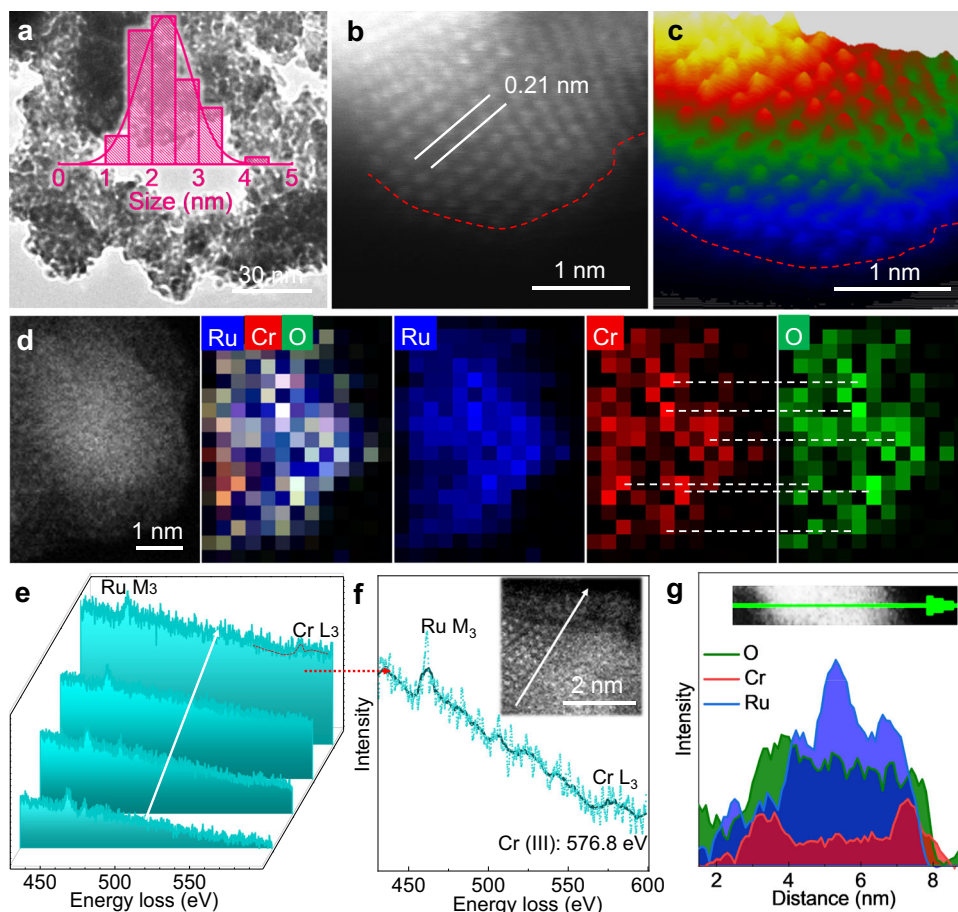


Fig. 2 | Structural characterizations of Ru-Cr₁(OH)_x. **a** TEM image. Inset is the size distribution of nanoparticles. High-resolution HAADF-STEM image (**b**) and the corresponding pseudo-color surface plot (**c**). **d** EELS mapping images. The line scanning EELS spectra (**e**) and the enlarged EELS spectra for the edge of Ru particle

(**f**). Inset in **f** is the line scanning path in the STEM-HAADF image. **g** EDS line-scanning profile across the nanoparticle and the corresponding HAADF-STEM image (inset).

with hydroxyl/oxygen clusters is successfully constructed on Ru nanoparticle for Ru-Cr₁(OH)_x, which will be further dissected by other technologies below. In addition, pure Ru nanoparticles (NPs) and other Ru-Cr₁(OH)_{x-y} samples (*y*% is the weight fraction of Cr) of Ru-Cr₁(OH)_{x-0.6} and Ru-Cr₁(OH)_{x-2.2} were also synthesized (Supplementary Figs. 8–11).

X-ray absorption spectroscopy was further performed to uncover the detailed structure of the atomically dispersed Cr₁(OH)_x species. As shown in Fig. 3a, the Cr K-edge X-ray absorption near-edge structure (XANES) spectra indicate that the three as-synthesized catalysts show a stronger pre-edge peak A (inset in Fig. 3a) and a larger intensity ratios for peaks B and C (*I_B/I_C*) than those for Cr(OH)₃. The profile differences suggest the existence of more distorted coordination structure of Cr-OH in Ru-Cr₁(OH)_x due to the atomic dispersion characteristic³³. In the Fourier transforms of the extended X-ray absorption fine-structure (FT-EXAFS) spectra, the peak at 2.42 Å between Cr-Cr (2.25 Å) and Cr-O-Cr (2.54 Å) can be well assigned to the Cr-Ru coordination (Fig. 3b). This is further confirmed by the least-squares EXAFS curve-fitting analysis for Cr-O, Cr-Ru and Cr-Cr coordination (Fig. 3c,d), which respectively shows the coordination numbers of 4.5, 1.5 and 0.6 for Ru-Cr₁(OH)_{x-1.1} with appropriate bond length and fitting parameters (Supplementary Table 2). The FT-EXAFS spectra along with the fitting results reveal that most Cr species are atomically dispersed on the Ru nanoparticles, whereas multimer chromium-oxygen (Cr-O-Cr) is less populated (<10%, Supplementary Table 2)³⁴. As expected, the ratio of the isolated Cr₁(OH)_x is decreased with increasing the loading of Cr species in Ru-Cr₁(OH)_x samples (Supplementary Fig. 12 and

Supplementary Table 2). Wavelet transform (WT) of EXAFS (Fig. 3e, Supplementary Fig. 13) can help distinguish the type of backscattering atoms. Ru-Cr₁(OH)_{x-1.1} exhibits one weak signal at >8.0 Å⁻¹ in *k* space that corresponds to the Cr-Ru coordination because of the higher atomic number of Ru. In contrast, the Cr-Cr in Cr foil and Cr-O-Cr in bulk Cr₂O₃ and Cr(OH)₃ at 7–8 Å⁻¹ in *k* space are not observed in Ru-Cr₁(OH)_{x-1.1}, further suggesting that the Cr₁(OH)_x species are atomically anchored on the metallic Ru surface, consistent with the above quantitative EXAFS analysis. On the other hand, the Ru-K-edge XANES and FT-EXAFS spectra of Ru-Cr₁(OH)_x samples show comparable metallic characteristic with that of pure Ru nanoparticles (Supplementary Fig. 14). In addition, the Cr K-edge XANES simulation for Ru-Cr₁(OH)_{x-1.1} was also carried out, and the calculated XANES matches very well with the collected spectroscopy (Supplementary Fig. 15), further verifying the proposed structure of atomically dispersed Cr₁(OH)_x species on Ru surface.

As shown in the near-edge X-ray absorption fine-structure (NEXAFS) spectra collected at O K edge (Fig. 4a), the characteristic peaks between 528–535 eV can be attributed to the spectroscopic excitations to the hybridized state of O 2*p* and Cr 3*d*, which can be divided into the *t*_{2g} and *e*_g orbital peaks³⁵. The pronounced feature at 529.2 eV is ascribed to the Cr-deficient sites and disordered environment due to the oxygen-rich Cr₁(OH)_x clusters in Ru-Cr₁(OH)_x³⁶. In addition, both the intensity and position of the *e*_g orbital peaks for Ru-Cr₁(OH)_x samples exhibit different profiles compared to Cr₂O₃ and Cr(OH)₃, confirming the distinct oxygen species in single Cr₁(OH)_x clusters. The Cr L_{II,III}-edge NEXAFS spectra show the anchored Cr species present an

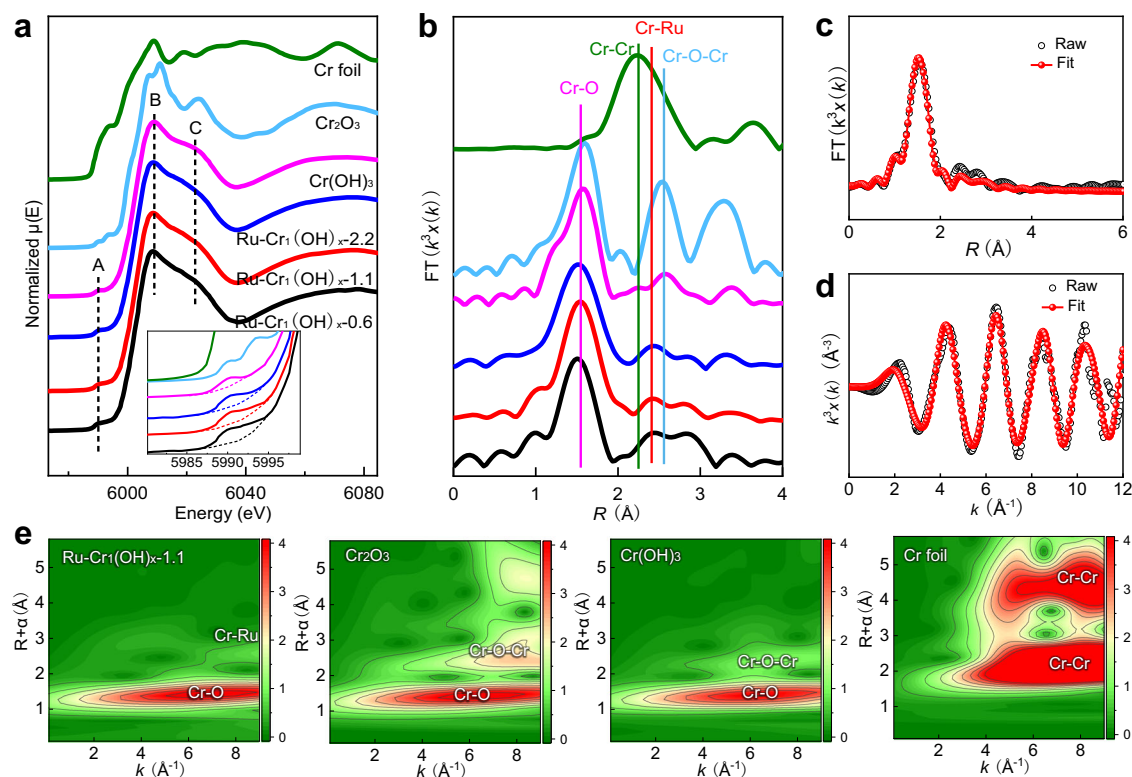


Fig. 3 | XAFS measurements of different samples at the Cr K-edge. **a** XANES spectra. The inset displays a magnified view of the pre-edge peak A. **b** k^3 -weighted

FT-EXAFS spectra in R -space. EXAFS fitting curves of Ru-Cr₁(OH)_{x-1.1} in R (**c**) and k (**d**) space. **e** WT for the k^3 -weighted EXAFS of different samples.

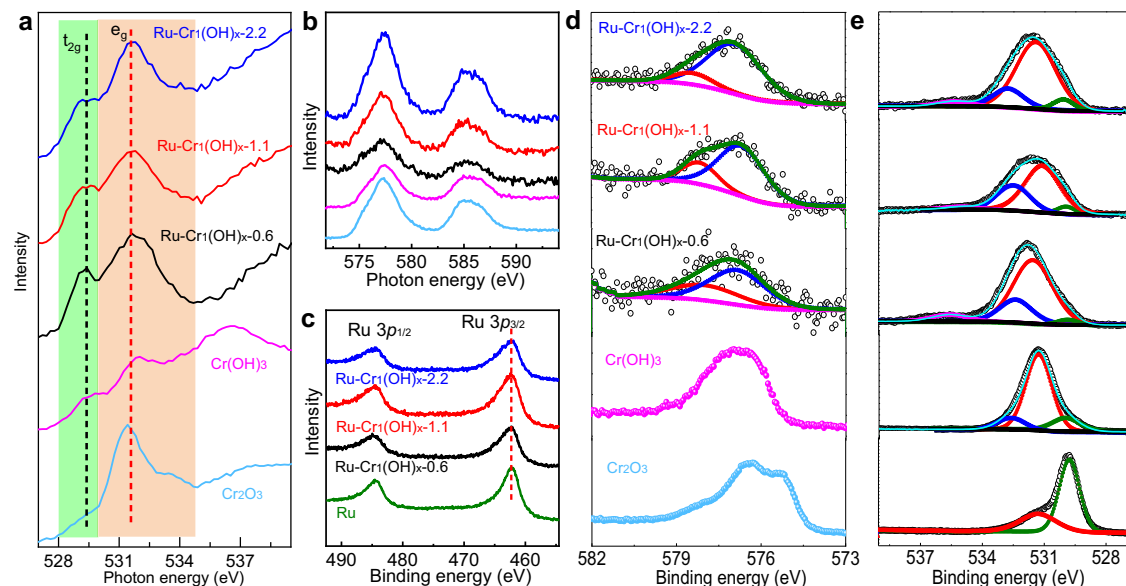


Fig. 4 | Fine structural characterizations. O K (**a**) and Cr L_{III} (**b**) edges NEXAFS spectra. Ru 3p (**c**), Cr 2p (**d**) and O 1s (**e**) XPS spectra.

identical Cr (III) state as compared to Cr₂O₃ and Cr(OH)₃ (Fig. 4b). X-ray photoelectron spectra (XPS) show that the ratios of Cr to Ru are larger than those determined by ICP, because Cr₁(OH)_x are anchored on Ru surface (Supplementary Table. 1). The Ru 3p_{3/2} binding energy for all Ru-based catalysts is around 462.3 eV, indicating that the oxidation state of Ru is not obviously changed after the incorporation of Cr species (Fig. 4c), in good agreement with the XAFS results. As shown in Fig. 4d, the Cr 2p_{3/2} binding energy in the Ru-Cr₁(OH)_x samples shifts

positively by ~0.9 eV and -0.4 eV compared with those of Cr₂O₃ and Cr(OH)₃, respectively. The Cr 2p_{3/2} XPS spectra of Ru-Cr₁(OH)_x samples can be fitted into two chemical states. The one located at 576.8 eV is assigned to Cr (III) trivalent hydroxide state and the other one at 578.3 eV is considered to be Cr (III) coordinated with additional hydroxyl ligands in Cr₁(OH)_x³⁷. More hydroxyl ligands are attached to Cr in Cr₁(OH)_x, which can well elucidate the increased binding energy of Cr 2p_{3/2}. The fraction of the peak at 578.3 eV is increased from

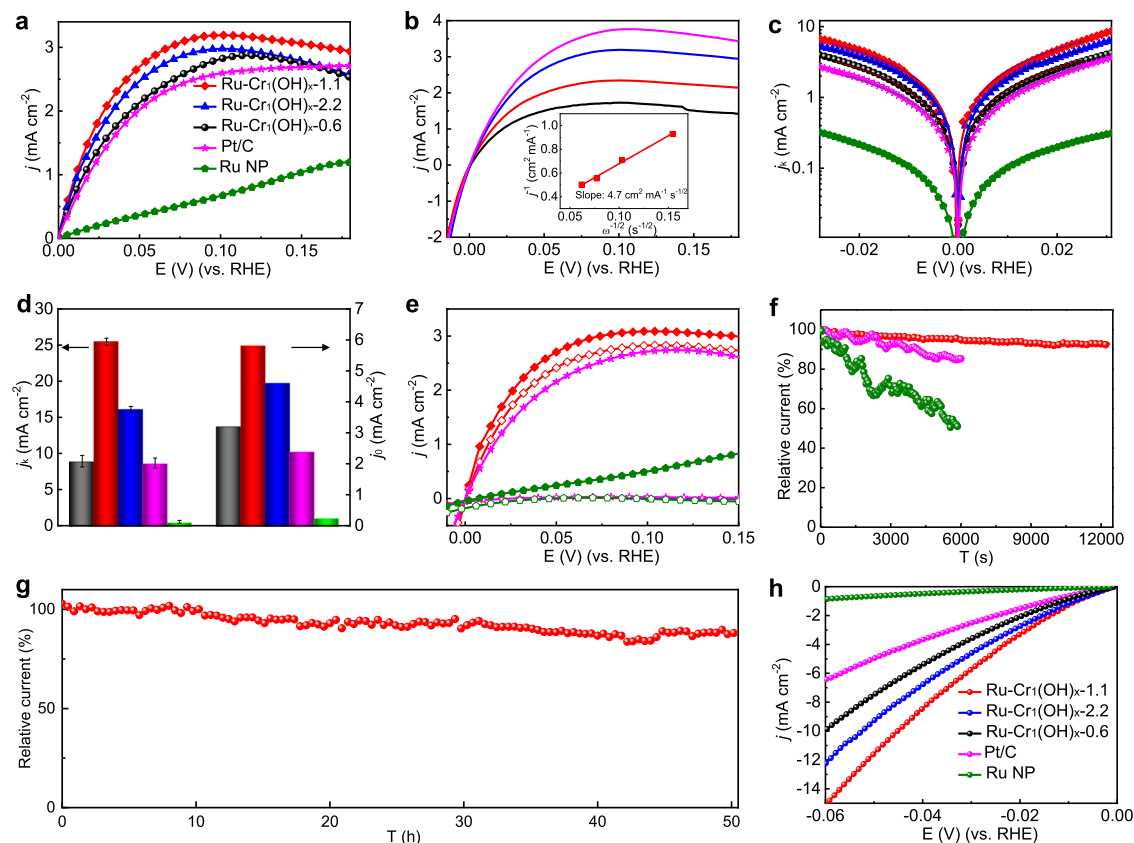


Fig. 5 | Electrochemical HOR performance. **a** HOR polarization curves of different catalysts. **b** Polarization curves of Ru-Cr₁(OH)_x-1.1 at different rotation speeds (ω) of 400, 900, 1600, and 2500 rpm (from bottom to top). Inset is the Koutecký–Levich plot at an overpotential of 25 mV. **c** Calculated HOR kinetic current densities (j_k) vs. potential plots recorded from **a**. **d** Comparison of j_k and j_0 of Ru-Cr₁(OH)_x-0.6 (black), Ru-Cr₁(OH)_x-1.1 (red), Ru-Cr₁(OH)_x-2.2 (blue), Ru NPs (green), and Pt/C (pink). Error bars show as mean s.d. **e** HOR polarization curves for

Ru-Cr₁(OH)_x-1.1 (red), Ru NPs (green) and Pt/C (pink) in H₂-saturated 0.1 M KOH without (solid lines) and with (dashed lines) the presence of 20,000 p.p.m. CO. **f** Relative current-time chronoamperometry of different catalysts at an overpotential of 50 mV operated on RDE. **g** Relative current-time chronoamperometry response of Ru-Cr₁(OH)_x-1.1 catalyst loaded on carbon fiber paper at an overpotential of 50 mV in a H-type cell. **h** HER polarization curves in 0.1 M KOH solution at a rotating speed of 1600 rpm.

Ru-Cr₁(OH)_x-2.2 to Ru-Cr₁(OH)_x-0.6, consistent with the result that the atomically dispersed Cr species are coordinated with more hydroxyl ligands. Accordingly, Ru-Cr₁(OH)_x samples exhibit a broad O 1s peak at -532.0 eV, which exhibits a positive shift compared to the other two references (Fig. 4e) and can be further divided into Cr-O-Cr (-529.9 eV), Cr-OH (-531.2 eV) and adsorbed H₂O (-532.6 eV). The content of Cr-O-Cr decreased dramatically from Cr₂O₃ (70.0%) and Cr(OH)₃ (14.4%) to Ru-Cr₁(OH)_x-0.6 (3.0%), Ru-Cr₁(OH)_x-1.1 (4.7%) and Ru-Cr₁(OH)_x-2.2 (6.3%), further validating the Cr-O-Cr bonds are largely broken so that more exposed oxygen atoms are formed in Cr₁(OH)_x clusters. All of the above results confirm the presence of abundant active oxygen species in the atomically dispersed Cr₁(OH)_x clusters, which would enable a unique catalytic process with faster kinetics compared with the typical nanoscale metal-support interfaces.

Electrocatalytic performance toward alkaline HOR

The electrocatalytic performance was evaluated by a rotating disk electrode (RDE) with a standard three-electrode system. The HOR polarization curves were obtained in a H₂-saturated 0.1 M KOH electrolyte at 25 °C and ambient pressure with a rotating speed of 1600 rpm. The current densities of Ru-Cr₁(OH)_x catalysts are significantly enhanced compared with pure Ru nanoparticles (Fig. 5a), indicating the atomically dispersed Cr₁(OH)_x species play a vital role in improving the HOR activity. In particular, the Ru-Cr₁(OH)_x-1.1 catalyst has much lower half-wave potential (20 mV) than those of Pt/C (27 mV) and Ru NPs (88 mV) (Supplementary Table 3). With increasing the rotation speed (ω), the current density of Ru-Cr₁(OH)_x-1.1 presents a linear

relationship (Levich plot) between the j^{-1} and $\omega^{-1/2}$ with calculated slope of $4.7 \text{ cm}^2 \text{ mA}^{-1} \text{ s}^{-1/2}$ (Fig. 5b), which is close to the theoretical value of $4.87 \text{ cm}^2 \text{ mA}^{-1} \text{ s}^{-1/2}$ for the two-electron HOR. HOR/HER Tafel plots of the kinetic current density (j_k) are then calculated based on the Koutecký–Levich equation (Fig. 5c), indicating the Ru-Cr₁(OH)_x-1.1 shows the highest kinetic activity over the potential range among all the presented catalysts. Figure 5d shows the j_k at 50 mV and the exchange current densities (j_0) extracted by fitting j_k according to the Butler–Volmer equation. The Ru-Cr₁(OH)_x-1.1 catalyst possesses the highest kinetic current density of 25.5 mA cm^{-2} , which is 51, 3.0, 2.9 and 1.6 times as high as those of Ru NPs (0.5 mA cm^{-2}), Pt/C (8.6 mA cm^{-2}), Ru-Cr₁(OH)_x-0.6 (8.9 mA cm^{-2}) and Ru-Cr₁(OH)_x-2.2 (16.1 mA cm^{-2}), respectively. The geometric j_0 of Ru-Cr₁(OH)_x-1.1 (5.8 mA cm^{-2}) is also significantly higher than those of Ru NPs (0.26 mA cm^{-2}), Pt/C (2.4 mA cm^{-2}), Ru-Cr₁(OH)_x-0.6 (3.2 mA cm^{-2}) and Ru-Cr₁(OH)_x-2.2 (4.6 mA cm^{-2}). The intrinsic HOR activities were further normalized by the electrochemically active surface area (ECSA) that was determined by copper underpotential deposition (Cu-UPD) cyclic voltammetry (Supplementary Figs. 16 and 17 and Supplementary Table 3), and the Ru-Cr₁(OH)_x-1.1 catalyst still exhibits the highest specific activity. The above results strongly suggest that incorporation of appropriate Cr₁(OH)_x clusters on Ru surface can significantly contribute to the improvement of HOR activity, while the formation of multimer chromium-oxygen clusters in Ru-Cr₁(OH)_x-2.2 is unfavorable to activity enhancement.

CO anti-poisoning ability is another important concern for HOR electrocatalysts in practical AEMFCs fueled by hydrogen from fossil

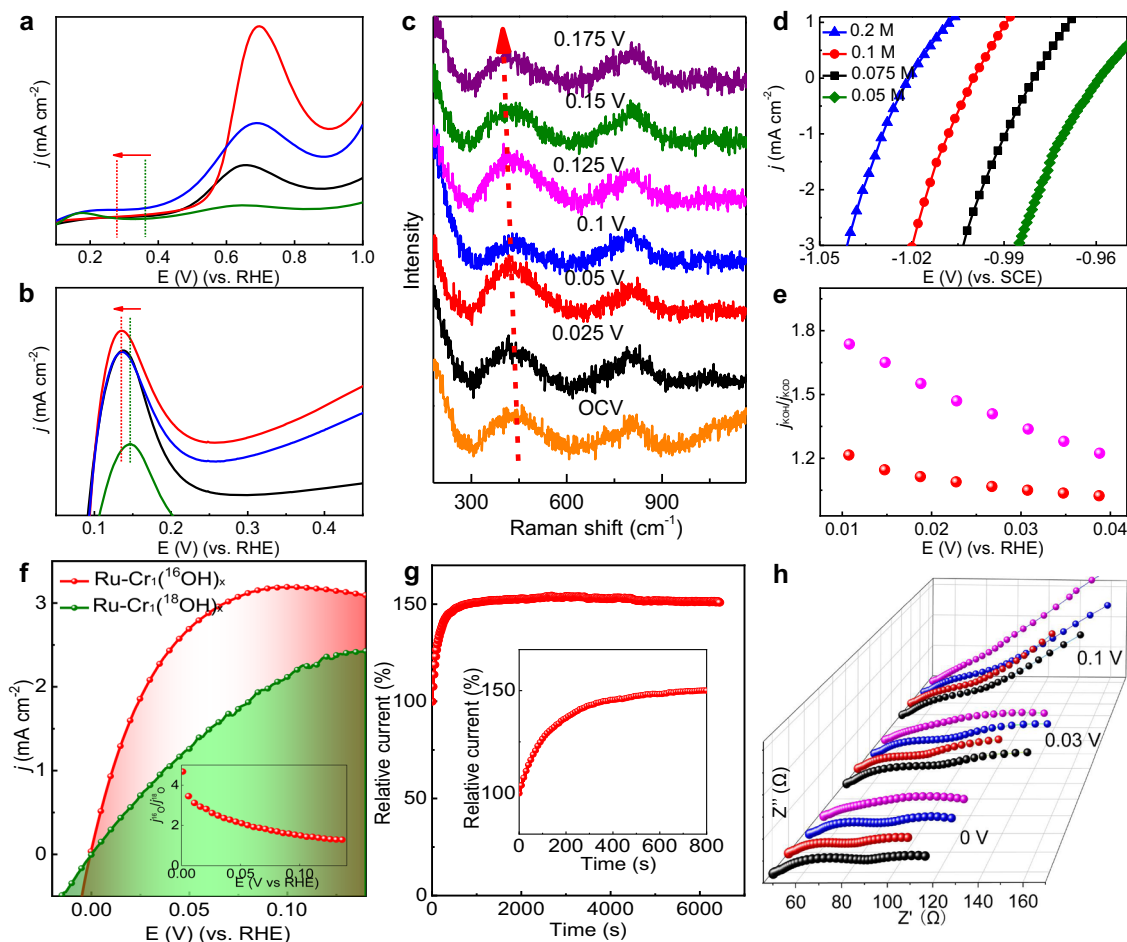


Fig. 6 | Mechanism investigation. CO-stripping (a) and $H_{\text{up,d}}$ (b) measurements for Ru-Cr₁(OH)_x-0.6 (black), Ru-Cr₁(OH)_x-1.1 (red), Ru-Cr₁(OH)_x-2.2 (blue), and Ru NPs (green). c In situ Raman spectra of Ru-Cr₁(OH)_x-1.1 at different overpotentials. d LSV curves of Ru-Cr₁(OH)_x-1.1 for HOR in different pH conditions. e H/D isotope effect analysis ($j_{\text{KOH}}/j_{\text{KOD}}$ vs. potential) for Ru-Cr₁(OH)_x-1.1 (red) and Pt/C (pink) in

0.1 M KOH/KOD electrolyte. f HOR polarization curves of Ru-Cr₁(¹⁸OH)_x and Ru-Cr₁(¹⁶OH)_x catalysts, inset is the corresponding current ratios of Cr₁(¹⁸OH)_x and Ru-Cr₁(¹⁸OH)_x. g Relative current-time chronoamperometry of Ru-Cr₁(¹⁸OH)_x catalysts at an overpotential of 50 mV. h Operando EIS of Ru-Cr₁(OH)_x-0.6 (black), Ru-Cr₁(OH)_x-1.1 (red), Ru-Cr₁(OH)_x-2.2 (blue), and Pt/C (pink).

fuels. Interestingly, Ru-Cr₁(OH)_x-1.1 shows exceptional HOR activity in the presence of CO, whereas both Pt/C and Ru NPs lose the HOR activity rapidly under the same test condition (Fig. 5e and Supplementary Fig. 18). The results indicate that the atomically dispersed Cr₁(OH)_x species play an important role in preventing CO poisoning in the HOR process. The large amount of active oxygen species in Cr₁(OH)_x clusters could assist the fast oxidation of CO on Ru surface, resulting in notable CO-tolerance performance. With regard to the catalytic durability, the HOR current density for Ru-Cr₁(OH)_x-1.1 at 50 mV shows a slight decay of 7% during continuous RDE test for 12000s (Fig. 5f), and, notably, the morphology, composition and structure of the catalyst were well maintained after durability evaluation (Supplementary Figs. 19 and 20). By contrast, Ru NPs and Pt/C suffer obvious activity degradation of 45% and 15% in current density after only 6000 s, respectively, mainly resulting from the agglomeration of active sites during the test (Supplementary Fig. 21). The Ru-Cr₁(OH)_x-1.1 catalyst was further deposited onto carbon papers in order to mitigate the loss of catalyst under the RDE testing condition¹⁰, and only shows -12% activity loss after 50-h durability test in a H-type cell (Fig. 5g). The results imply that the presence of Cr₁(OH)_x clusters can efficiently suppress the agglomeration and degradation of active sites during the HOR process³¹. As shown in Fig. 5h, the Ru-Cr₁(OH)_x-1.1 also exhibits the highest HER catalytic activity with an overpotential of 45 mV to reach 10 mA cm⁻², which is superior to those of Ru-Cr₁(OH)_x-2.2 (53 mV) and Ru-Cr₁(OH)_x-0.6 (60 mV).

Mechanism investigation

To reveal the mechanism of the highly catalytic activity of Ru derived from the Cr₁(OH)_x clusters, a series of experiments including electrochemistry, isotope-labeling and in situ Raman spectroscopy were conducted. CO stripping experiment (Fig. 6a and Supplementary Fig. 22) displays that the onset potential of CO stripping for Ru-Cr₁(OH)_x catalysts (-0.25 V) is substantially lower than those of Ru NPs (0.36 V) and Pt/C (0.54 V), suggesting the enhanced OHBE of Ru-Cr₁(OH)_x samples and the largely accelerated CO oxidation triggered by the hydroxyl on Cr₁(OH)_x³⁸. On the other hand, the position of hydrogen underpotential deposition ($H_{\text{up,d}}$) peak (Fig. 6b) shows that the desorption peak position (-0.135 V) for Ru-Cr₁(OH)_x catalysts is lower than those of Ru NPs (0.147 V) and Pt/C (0.291 V), revealing the weakened Ru-H binding³⁹. The above HBE influenced by the Cr₁(OH)_x clusters was further explored by in situ Raman spectroscopy (Fig. 6c, Supplementary Fig. 23). The broad feature at 810 cm⁻¹ can be ascribed to symmetric and anti-symmetric Cr-OH stretching, while the feature at 440 cm⁻¹ is assigned to Cr-O-H bending mode⁴⁰. With increasing the overpotential from open circuit voltage (OCV) to 175 mV during the HOR process, a red shift becomes more and more pronounced for the peak associated with Cr-O-H bending mode, which could be attributed to the hydrogen spillover from Ru surface to the active oxygen species of Cr₁(OH)_x^{41,42}. The active oxygen species of Cr₁(OH)_x clusters for shuffling the hydrogen is further confirmed by the increased pH of ultrapure water after dispersing Ru-Cr₁(OH)_x powders

(Supplementary Fig. 24)³⁶. The above results indicate the unique oxygen species in $\text{Cr}_1(\text{OH})_x$ can facilitate interact with the hydrogen adsorbed on Ru surface, resulting in optimized HBE, which simultaneously promotes the Volmer step.

The role of oxygen species in HOR process was further investigated in detail. The $\text{Ru-Cr}_1(\text{OH})_{x-1.1}$ catalyst exhibits a similar kinetic activity of HOR in 0.05 M to 0.2 M KOH (Fig. 6d), which is different from the behaviors of Pt/C (Supplementary Fig. 25), suggesting the $\text{Cr}_1(\text{OH})_x$ clusters have strong capacity in providing enough reactive hydroxyl species in alkaline media. The HOR activity of $\text{Ru-Cr}_1(\text{OH})_x$ catalyst has an H/D isotope effect of 1.0–1.2 influenced by the applied potentials (Fig. 6e), whereas Pt/C possesses an H/D isotope effect of 1.2–1.7. The results indicate that the OH^- substituted by OD^- in the electrolyte will reduce the HOR activity because hydroxyl participates in the HOR process⁴³. However, the $\text{Ru-Cr}_1(\text{OH})_x$ catalyst is less affected in the process, implying the $\text{Cr}_1(\text{OH})_x$ clusters can also adsorb OD^- efficiently for further reaction due to their unique role in constructing active oxygen species, which is consistent with the results of pH dependence of HOR activity. The active oxygen species in $\text{Cr}_1(\text{OH})_x$ clusters for HOR were further examined via kinetic isotope effect (KIE) studies by ^{18}O -labeled $\text{Cr}_1(^{18}\text{OH})_x$ in the catalysts, which were obtained by substituting H_2^{18}O for H_2O in the synthesis process. The HOR kinetics of $\text{Ru-Cr}_1(^{18}\text{OH})_x$ is much slower than that of $\text{Ru-Cr}_1(^{16}\text{OH})_x$ (Fig. 6f), indicating that the hydroxyl species of $\text{Cr}_1(^{18}\text{OH})_x$ participate in the rate-determining step of the HOR since their mass increases upon the substitution. When the ^{18}OH in the clusters is gradually substituted by the ^{16}OH during the HOR process, the HOR kinetics would be recovered accompanied with the formation of H_2^{18}O (Fig. 6g, Supplementary Fig. 26), further confirming the original active hydroxyl in the $\text{Cr}_1(\text{OH})_x$ clusters participates in the reaction step of HOR.

The higher HOR activity of $\text{Ru-Cr}_1(\text{OH})_{x-1.1}$ compared with the other two samples ($\text{Ru-Cr}_1(\text{OH})_{x-0.6}$ with lower density of $\text{Cr}_1(\text{OH})_x$ and $\text{Ru-Cr}_1(\text{OH})_{x-2.2}$ with multimer chromium-oxygen clusters as confirmed in Fig. 3) is investigated by operando electrochemical impedance spectroscopy (EIS). $\text{Ru-Cr}_1(\text{OH})_{x-1.1}$ shows a smaller low-frequency-dominant specific resistance from low to high overpotentials (Fig. 6h), suggesting the higher activity of per active site. The Nyquist plots are fitted by a double-parallel equivalent circuit model (Supplementary Figs. 27 and 28 and Supplementary Table 4)⁴⁴. The first and second parallel component represent the charge transfer resistance R_1 and hydrogen adsorption resistance R_2 . EIS-derived Tafel curves of charge transfer kinetics and hydrogen adsorption kinetics clearly show that the R_1 and R_2 of $\text{Ru-Cr}_1(\text{OH})_{x-1.1}$ are lower than the other two samples (Supplementary Fig. 29). It also suggests that the Tafel slopes of $\log R_1$ and $\log R_2$ vs. overpotential for $\text{Ru-Cr}_1(\text{OH})_{x-1.1}$ are lower and close to those of $\text{Ru-Cr}_1(\text{OH})_{x-0.6}$ and $\text{Ru-Cr}_1(\text{OH})_{x-2.2}$, respectively, indicating the $\text{Ru-Cr}_1(\text{OH})_{x-1.1}$ catalyst balances the hydrogen adsorption and charge transfer kinetics. The above results reveal the appropriate coverage of isolated $\text{Cr}_1(\text{OH})_x$ on $\text{Ru-Cr}_1(\text{OH})_{x-1.1}$ rather than multimer chromium-oxygen clusters on heterostructure catalyst is beneficial to achieve the optimized active sites for efficient hydrogen spillover and charge transfer.

Theoretical simulations

To further verify the proposed mechanism, density functional theory (DFT) calculations were performed on the two models of Ru (001) surfaces anchored by isolated $\text{Cr}_1(\text{OH})_x$ and multimer chromium-oxygen ($\text{Cr}_m(\text{OH})_x$) clusters. The model surface is commonly observed and adopted both in experimental (Fig. 2b) and theoretical studies^{45,46}, although it is a challenge to fully address all the surface sites under real experimental situation. The $\text{Cr}_1(\text{OH})_x$ model is established according to the EXAFS fitting results (Supplementary Table 2) and the $\text{Cr}_m(\text{OH})_x$ model is extracted from chromium hydroxide (Supplementary

Fig. 30). The density of states (DOS) of O 2p indicate that the O 2p-band center of $\text{Ru-Cr}_1(\text{OH})_x$ is closer to the Fermi level compared with that of $\text{Ru-Cr}_m(\text{OH})_x$, suggesting that the oxygen species of $\text{Ru-Cr}_1(\text{OH})_x$ are more feasible to interact with the H_{ad} intermediates (Fig. 7a). The result also implies that the construction of isolated $\text{Cr}_1(\text{OH})_x$ clusters is important to create more active oxygen species than the typical (hydr)-oxide nanoparticles, in accordance with above operando EIS investigations. The more negative charge of the oxygen species in $\text{Ru-Cr}_1(\text{OH})_x$ further reflects the stronger basicity for capturing protons over those in $\text{Cr}_m(\text{OH})_x$ (Fig. 7b, Supplementary Fig. 31), consistent with the NEXAFS, XPS and in situ Raman results (Figs. 4 and 6). The unique active oxygen species of $\text{Ru-Cr}_1(\text{OH})_x$ are thus expected to interact with the adsorbed hydrogen on Ru surface and thus lower the HBE. As shown in Fig. 7c and Supplementary Fig. 32, $\text{Cr}_1(\text{OH})_x$ can largely increase the hydrogen adsorption energy on Ru surface to 0.2 eV, which is much higher than those of $\text{Ru-Cr}_m(\text{OH})_x$ (−0.22 eV), Ru (−0.04 eV) and Pt (−0.31 eV)¹². With such reduced HBE induced by $\text{Cr}_1(\text{OH})_x$, hydrogen spillover from Ru surface to $\text{Cr}_1(\text{OH})_x$ can be easily achieved. As a result, the hydroxyl from $\text{Ru-Cr}_1(\text{OH})_x$ reacts with the adsorbed hydrogen in the rate-determining Volmer step for $^*\text{H} + ^*\text{OH} \rightarrow \text{H}_2\text{O}$ with an energy barrier of only 0.33 eV (Fig. 7d-f, Supplementary Fig. 33), which is greatly decreased compared to $\text{Ru-Cr}_m(\text{OH})_x$ (0.67 eV). The energy barrier for the Volmer step of $\text{Ru-Cr}_1(\text{OH})_x$ is also much lower than the reported Ru or Pt-based catalysts, which usually have energy barriers higher than 1.0 eV^{17,47}. All the above experimental and calculation results demonstrate that the isolated $\text{Cr}_1(\text{OH})_x$ clusters on the Ru surface introduce unique active oxygen species, which could shuffle the H_{ad} intermediates for appropriate HBE and greatly promote hydrogen spillover from Ru to the hydroxyl of $\text{Cr}_1(\text{OH})_x$, eventually participating in and accelerating the Volmer step of H_2O formation for faster alkaline HOR kinetics.

In summary, constructing atomically dispersed $\text{Cr}_1(\text{OH})_x$ on Ru surface was proposed to maximize the number of interfacial reactive sites and create a unique HOR pathway, eventually enabling efficient hydrogen oxidation. The active oxygen species activated by $\text{Cr}_1(\text{OH})_x$ are specific for optimizing the hydrogen adsorption on Ru surface and greatly promoting hydrogen spillover from Ru to $\text{Cr}_1(\text{OH})_x$. For further accelerated oxidation process, the original oxygen species from $\text{Cr}_1(\text{OH})_x$ and activated oxygen species from electrolyte are both confirmed to participate in the H_2O production of Volmer step. Meanwhile, excellent durability and CO anti-poisoning ability are also achieved because the isolated $\text{Cr}_1(\text{OH})_x$ clusters are conducive to removing the CO molecules and suppressing the aggregation of Ru species during HOR. The findings suggest that, as compared with typical metal (hydr)oxide nano-interface, atomic/cluster-level interface with unique physicochemical properties would ensure intrinsically enhanced electrocatalytic performance, which also opens a new avenue for the development of advanced catalysts via interface and/or surface engineering.

Methods

Synthesis of $\text{Ru-Cr}_1(\text{OH})_x$

$\text{Ru-Cr}_1(\text{OH})_x$ samples were prepared via a facile one-step process using NaBH_4 -induced spontaneous gelation process. Take the synthesis of $\text{Ru-Cr}_1(\text{OH})_{x-1.1}$ as an example. First, 100 mg of $\text{RuCl}_3 \cdot x\text{H}_2\text{O}$ with a 12 mg of $\text{CrCl}_3 \cdot 6\text{H}_2\text{O}$ were dissolved in 20 mL deionized water by an ultrasound treatment. Then NaBH_4 aqueous solution (1M) of 4 mL was injected into the above solution under vigorous stirring. Until no bubbles formed, the obtained precipitates were subsequently washed with water to completely remove the undeposited Cr-based precursors. Finally, the obtained solid was immediately frozen in liquid nitrogen for 10 min, and then dried under freeze drying. $\text{Ru-Cr}_1(\text{OH})_{x-0.6}$ and $\text{Ru-Cr}_1(\text{OH})_{x-2.2}$ were prepared by a similar procedure but using $\text{CrCl}_3 \cdot 6\text{H}_2\text{O}$ of 3 mg and 24 mg, respectively.

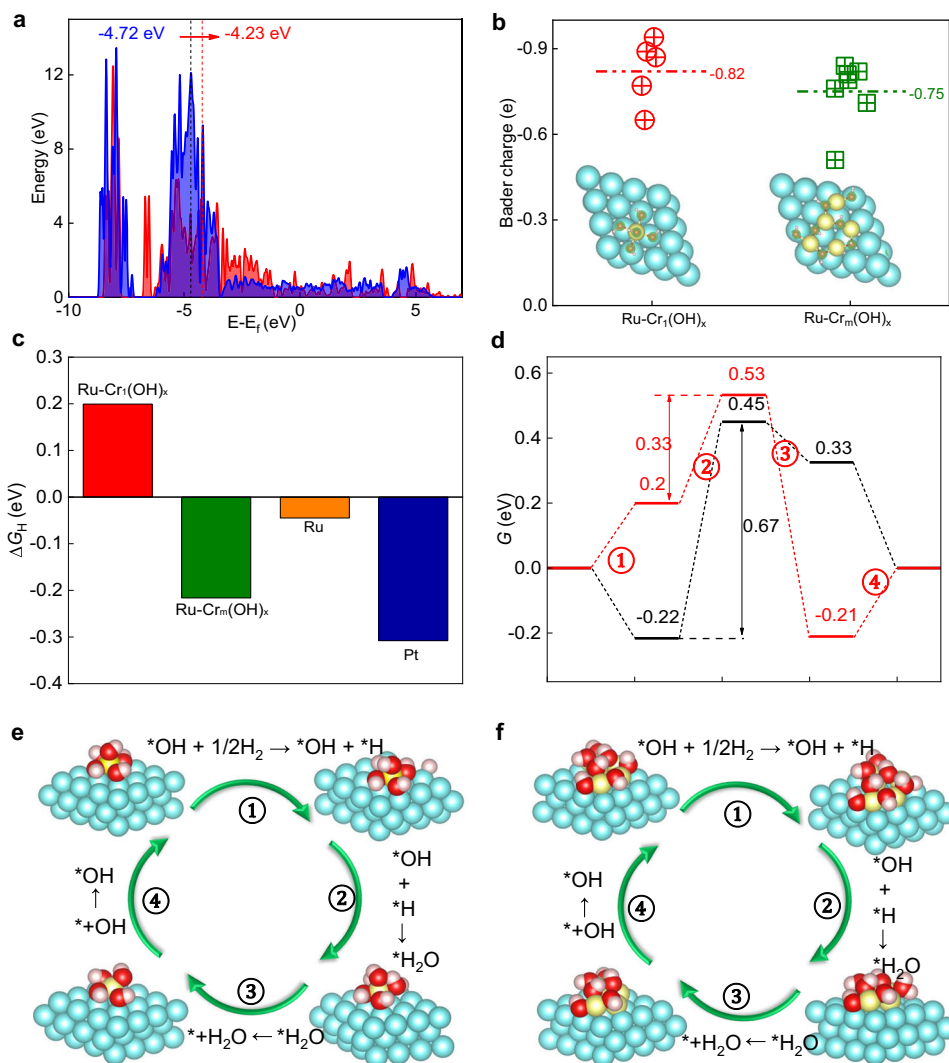


Fig. 7 | DFT calculation results. **a** DOS of O 2p for Ru-Cr₁(OH)_x (red) and Ru-Cr_m(OH)_x (blue). The dashed vertical lines represent the position of O 2p-band center. **b** Bader charge analysis of O atoms for Ru-Cr₁(OH)_x and Ru-Cr_m(OH)_x. The labeled number is the average Bader charge of O atoms. **c** Free energy for H

adsorption on different models. Free energy diagrams (**d**) of the elementary processes of HOR on Ru-Cr₁(OH)_x (red) and Ru-Cr_m(OH)_x (black) including atomic configurations of each states on Ru-Cr₁(OH)_x (**e**) and Ru-Cr_m(OH)_x (**f**). Color: blue, Ru; yellow, Cr; red, O; white, H.

Synthesis of Ru nanoparticle

Ru nanoparticles were synthesized following a similar procedure without addition of additional CrCl₃·6H₂O.

Synthesis of ¹⁸O labeled Ru-Cr₁(¹⁸OH)_x nanoparticles

First, 10 mg of RuCl₃·xH₂O with a 1.2 mg of CrCl₃·6H₂O were dissolved in 2 mL heavy-oxygen water by an ultrasound treatment. Then NaBH₄ (0.4 mmol) was added into the above solution under vigorous stirring. Until no bubbles formed, the obtained precipitates were subsequently washed with heavy-oxygen water to completely remove the undeposited Cr-based precursors. Then, the obtained solid was immediately frozen in liquid nitrogen for 10 min, and then dried under freeze drying. Finally, the dried sample was stored under vacuum oven.

Characterizations

The XRD patterns were collected using a RigakuDmax-rc X-ray diffractometer equipped with Cu Kα radiation (λ = 1.5418 Å). The morphologies of the samples were characterized by SEM (HITACHI SU-3500) and TEM (FEI Tecnai G² F20 S-TWIN). The HAADF-STEM was performed on a FEI Titan G² 60-300 equipped with a spherical aberration corrector. XPS spectra were acquired by VG Scientific

ESCALab220i-XL spectrometer using Al Kα photon source equipped with 500 μm X-ray spot, and the base pressure in the analysis chamber was controlled to be 3 × 10⁻¹⁰ mbar. The Raman spectra were measured using a laser confocal fiber Raman spectrometer (Renishaw inVia-Reflex). Elemental analysis of the samples was performed with ICP-OES (ICAP-RQ, ThermoFisher Scientific, Germany). The NEXAFS spectra of the samples were collected at beamline BL10B in the National Synchrotron Radiation Laboratory (NSRL) in Hefei, China. The measurements of X-ray absorption spectroscopy were performed at beamline BL14W1 in the Shanghai Synchrotron Radiation Facility. Data processing of XANES and EXAFS was carried out with the Athena and Artemis modules of the IFFFIT software package. The spectra were normalized, background removed and corrected according to the first and largest peak of the first derivative of XANES. *k*³-weighting and a *R*_{bkg} value of 1.0 were selected for the data processing. The quantitative structural parameters were obtained using a least-squares curve parameter fitting for the EXAFS spectra by ARTEMIS module. The ab initio XANES simulations of Cr K-edge XANES spectra were performed via the MXAN package, which can quantitatively analyze the XANES spectra via comparing experimental data and theoretical calculations with adjusted geometrical parameters at the photon absorber site⁴⁸.

The calculations of X-ray absorption cross-sections were carried out using the full multiple scattering approach with the muffin-tin (MT) approximation for the potential shape⁴⁹. The optimized Cr coordinated with five oxygen atoms on Ru (001) determined by DFT calculations (Supplementary Fig. 30a) was employed as the initial structure.

Electrochemical measurements

Electrocatalytic measurements were performed in a standard three-electrode cell system using an electrochemical station (Chi 760E). A glassy carbon electrode (GCE) with a diameter of 5 mm, graphite rod and Hg/HgO electrode were used as the working electrode, counter electrode and reference electrode, respectively. Before the electrochemical test, the GCE was consecutively polished with Al₂O₃ slurry with particle size of 50 nm, then washed with ethanol and water to obtain a clean surface. The catalyst ink was prepared by dispersing 0.4 mg catalysts and 1.6 mg of VulcanXC-72 in a mixed solution including 490 μL of ethanol and 10 μL of 5% Nafion solution. The above suspensions were sonicated for 1 h to obtain a homogeneous ink. Then, the electrocatalyst ink was dropped onto the GCE surface with loading of 0.06 mg_{metal} cm⁻². After being dried, the working electrode was firstly cycled between -0.1 and -0.3 V vs. RHE at a scan rate of 200 mV s⁻¹ for 5 cycles. HOR tests were carried out in H₂-saturated KOH solution (0.1M) with 95% iR correction and recorded at a rotation speed of 1,600 rpm with a scanning rate of 2 mV/s. The durability tests were performed in 0.1M KOH solution by chronoamperometry experiments with carbon fiber paper (catalyst loading: -2 mg cm⁻²) as the working electrode.

The kinetic current (j_k) was calculated based on the Koutecky–Levich equation:

$$1/j = 1/j_k + 1/j_D \quad (1)$$

where j stands for the measured current and j_D represents the diffusion current.

The specific exchange current density (j_0) was obtained by fitting j_k with Butler–Volmer equation:

$$j_k = j_0 [e^{(\alpha F/RT)} \eta - e^{-(1-\alpha)F/RT}] \eta \quad (2)$$

where α is the charge transfer coefficient, R is the universal gas constant (8.314 J mol⁻¹ K⁻¹), and T is the temperature (K), α and j_0 were set as variables.

The electrochemical impedance spectroscopy was measured at different overpotentials and an amplitude of the sinusoidal voltage of 5 mV with a frequency range of 100 kHz to 100 mHz.

CO stripping was firstly performed with amperometric i-t test at 0.05 V vs. RHE for 10 min in a CO-saturated 0.1M KOH solution for CO adsorption. Then the electrode was transferred into a N₂-saturated 0.1M KOH solution. The CO stripping current was obtained by CV in the potential range of 0–1.0 V vs. RHE and at a scan rate of 20 mV s⁻¹.

HOR tests of Ru–Cr₁(¹⁸OH)_x catalyst were performed in a micro electrolytic cell with the volume of 4 mL to concentrate the H₂¹⁸O produced from Ru–Cr₁(¹⁸OH)_x.

Computational details for calculations

All the spin-polarized DFT calculations on this system were performed by Vienna ab initio simulation package⁵⁰. The projector-augmented wave (PAW) method and Perdew–Burke–Ernzerhof (PBE)^{51,52} functional within the generalized gradient approximation (GGA) were used to describe ionic cores and exchange-correlation effects, respectively. A cutoff energy of 500 eV and the Grimme method for DFT-D3 were used to account for van der Waals (vdW) interactions⁵². The vacuum gap between periodic images was set to 15 Å to avoid interaction. The convergence criteria for residual force and energy were set to 0.05 eV/

Å and 10⁻⁵ eV, respectively. The Brillouin zone was applied by a 2 × 2 × 1 Gamma-centered special k points grid for geometry optimization. The free energy for HOR was calculated based on the computational hydrogen electrode (CHE) model proposed by Nørskov et al.⁵³. In this model, the free energy of proton–electron pair is equal to that of 1/2 H₂(g). The free energy change for each fundamental step was obtained by

$$\Delta G = \Delta E + E_{\text{ZPE}} - T\Delta S \quad (3)$$

where ΔE is the difference of electronic energy obtained from DFT simulation. ΔE_{ZPE} is the variation of zero-point energy (ZPE), ΔS is the entropy (S) change, T is the temperature ($T = 298.15$ K). For the molecular in gas phase, the ZPE and S were taken from NIST⁵⁴ database.

Data availability

The data supporting the findings of this study are available within the article and its Supplementary information files. All data is available from the authors upon reasonable request.

References

- Setzler, B. P., Zhuang, Z., Wittkopf, J. A. & Yan, Y. Activity targets for nanostructured platinum-group-metal-free catalysts in hydroxide exchange membrane fuel cells. *Nat. Nanotechnol.* **11**, 1020–1025 (2016).
- Varcoe, J. R. et al. Anion-exchange membranes in electrochemical energy systems. *Energy Environ. Sci.* **7**, 3135–3191 (2014).
- Zhao, G., Chen, J., Sun, W. & Pan, H. Non-platinum group metal electrocatalysts toward efficient hydrogen oxidation reaction. *Adv. Funct. Mater.* **31**, 2010633 (2021).
- Strmcnik, D. et al. Improving the hydrogen oxidation reaction rate by promotion of hydroxyl adsorption. *Nat. Chem.* **5**, 300–306 (2013).
- Ledezma-Yanez, I. et al. Interfacial water reorganization as a pH-dependent descriptor of the hydrogen evolution rate on platinum electrodes. *Nat. Energy* **2**, 17031 (2017).
- Sheng, W. et al. Correlating hydrogen oxidation and evolution activity on platinum at different pH with measured hydrogen binding energy. *Nat. Commun.* **6**, 5848 (2015).
- Sheng, W., Gasteiger, H. A. & Shao-Horn, Y. Hydrogen oxidation and evolution reaction kinetics on platinum: acid vs alkaline electrolytes. *J. Electrochem. Soc.* **157**, B1529 (2010).
- Duan, Y. et al. Bimetallic nickel–molybdenum/tungsten nanoalloys for high-efficiency hydrogen oxidation catalysis in alkaline electrolytes. *Nat. Commun.* **11**, 4789 (2020).
- Wang, M. et al. Alloying nickel with molybdenum significantly accelerates alkaline hydrogen electrocatalysis. *Angew. Chem. Int. Ed.* **60**, 5771–5777 (2021).
- Gao, L. et al. A nickel nanocatalyst within a h-BN shell for enhanced hydrogen oxidation reactions. *Chem. Sci.* **8**, 5728–5734 (2017).
- Wang, T. et al. Weakening hydrogen adsorption on nickel via interstitial nitrogen doping promotes bifunctional hydrogen electrocatalysis in alkaline solution. *Energy Environ. Sci.* **12**, 3522–3529 (2019).
- Zhu, S. et al. The role of ruthenium in improving the kinetics of hydrogen oxidation and evolution reactions of platinum. *Nat. Catal.* **4**, 711–718 (2021).
- Zhu, S., Qin, X., Yao, Y. & Shao, M. pH-Dependent hydrogen and water binding energies on platinum surfaces as directly probed through surface-enhanced infrared absorption spectroscopy. *J. Am. Chem. Soc.* **142**, 8748–8754 (2020).
- Shi, Y. et al. Atomic-level metal electrodeposition: synthetic strategies, applications, and catalytic mechanism in electrochemical energy conversion. *Small Struct.* **3**, 2100185 (2022).

15. Kweon, D. H. et al. Ruthenium anchored on carbon nanotube electrocatalyst for hydrogen production with enhanced Faradaic efficiency. *Nat. Commun.* **11**, 1278 (2020).
16. Mahmood, J. et al. An efficient and pH-universal ruthenium-based catalyst for the hydrogen evolution reaction. *Nat. Nano* **12**, 441–446 (2017).
17. Wang, Y.-H. et al. Spectroscopic verification of adsorbed hydroxy intermediates in the bifunctional mechanism of the hydrogen oxidation reaction. *Angew. Chem. Int. Ed.* **60**, 5708–5711 (2021).
18. Zhang, J. et al. Engineering the near-surface of PtRu₃ nanoparticles to improve hydrogen oxidation activity in alkaline electrolyte. *Small* **17**, 2006698 (2021).
19. Qin, S. et al. Ternary nickel–tungsten–copper alloy rivals platinum for catalyzing alkaline hydrogen oxidation. *Nat. Commun.* **12**, 2686 (2021).
20. Qiu, Y. et al. BCC-phased PdCu alloy as a highly active electrocatalyst for hydrogen oxidation in alkaline electrolytes. *J. Am. Chem. Soc.* **140**, 16580–16588 (2018).
21. Lu, S. & Zhuang, Z. Investigating the influences of the adsorbed species on catalytic activity for hydrogen oxidation reaction in alkaline electrolyte. *J. Am. Chem. Soc.* **139**, 5156–5163 (2017).
22. Zhao, T. et al. Self-optimized ligand effect in L₁₂-PtPdFe intermetallic for efficient and stable alkaline hydrogen oxidation reaction. *ACS Catal.* **10**, 15207–15216 (2020).
23. Xue, Y. et al. A highly-active, stable and low-cost platinum-free anode catalyst based on RuNi for hydroxide exchange membrane fuel cells. *Nat. Commun.* **11**, 5651 (2020).
24. Song, F. et al. Interfacing nickel nitride and nickel boosts both electrocatalytic hydrogen evolution and oxidation reactions. *Nat. Commun.* **9**, 4531 (2018).
25. Yang, F. et al. Boosting hydrogen oxidation activity of Ni in alkaline media through oxygen-vacancy-rich CeO₂/Ni heterostructures. *Angew. Chem. Int. Ed.* **58**, 14179–14183 (2019).
26. Yang, Y. et al. Enhanced electrocatalytic hydrogen oxidation on Ni/NiO/C derived from a nickel-based metal–organic framework. *Angew. Chem. Int. Ed.* **58**, 10644–10649 (2019).
27. Zhou, Y. et al. Lattice-confined Ru clusters with high CO tolerance and activity for the hydrogen oxidation reaction. *Nat. Catal.* **3**, 454–462 (2020).
28. Singh, R. K. et al. Synthesis of CeO_x-decorated Pd/C catalysts by controlled surface reactions for hydrogen oxidation in anion exchange membrane fuel Cells. *Adv. Funct. Mater.* **30**, 2002087 (2020).
29. Fu, L. et al. IrMo Nanocatalysts for efficient alkaline hydrogen electrocatalysis. *ACS Catal.* **10**, 7322–7327 (2020).
30. Hamo, E. R. et al. Carbide-supported PtRu catalysts for hydrogen oxidation reaction in alkaline electrolyte. *ACS Catal.* **11**, 932–947 (2021).
31. Speck, F. D. et al. Improved hydrogen oxidation reaction activity and stability of buried metal-oxide electrocatalyst interfaces. *Chem. Mater.* **32**, 7716–7724 (2020).
32. Cui, W. W. et al. Cr(III) Adsorption by cluster formation on boehmite nanoplates in highly alkaline solution. *Environ. Sci. Technol.* **53**, 11043–11055 (2019).
33. Yang, H. B. et al. Atomically dispersed Ni(i) as the active site for electrochemical CO₂ reduction. *Nat. Energy* **3**, 140–147 (2018).
34. Cao, L. et al. Atomically dispersed iron hydroxide anchored on Pt for preferential oxidation of CO in H₂. *Nature* **565**, 631–635 (2019).
35. Lee, W. H. et al. Electrode reconstruction strategy for oxygen evolution reaction: maintaining Fe-CoOOH phase with intermediate-spin state during electrolysis. *Nat. Commun.* **13**, 605 (2022).
36. Lu, K. et al. Li_xNiO/Ni Heterostructure with strong basic lattice oxygen enables electrocatalytic hydrogen evolution with Pt-like activity. *J. Am. Chem. Soc.* **142**, 12613–12619 (2020).
37. Yang, J., Baker, A. G., Liu, H., Martens, W. N. & Frost, R. L. Size-controllable synthesis of chromium oxyhydroxide nanomaterials using a soft chemical hydrothermal route. *J. Mater. Sci.* **45**, 6574–6585 (2010).
38. Shen, L.-f et al. Does the oxophilic effect serve the same role for hydrogen evolution/oxidation reaction in alkaline media? *Nano Energy* **62**, 601–609 (2019).
39. Ramaswamy, N. et al. Hydrogen oxidation reaction in alkaline media: Relationship between electrocatalysis and electrochemical double-layer structure. *Nano Energy* **41**, 765–771 (2017).
40. Gomes, A. S. O., Yaghini, N., Martinelli, A. & Ahlberg, E. A micro-Raman spectroscopic study of Cr(OH)₃ and Cr₂O₃ nanoparticles obtained by the hydrothermal method. *J. Raman Spectrosc.* **48**, 1256–1263 (2017).
41. Wei, Z. W. et al. Reversed charge transfer and enhanced hydrogen spillover in platinum nanoclusters anchored on titanium oxide with rich oxygen vacancies boost hydrogen evolution reaction. *Angew. Chem. Int. Ed.* **60**, 16622–16627 (2021).
42. Liu, X.-C. et al. Tailoring the electrochemical protonation behavior of CO₂ by tuning surface noncovalent interactions. *ACS Catal.* **11**, 14986–14994 (2021).
43. Liu, E. S. et al. Interfacial water shuffling the intermediates of hydrogen oxidation and evolution reactions in aqueous media. *Energy Environ. Sci.* **13**, 3064–3074 (2020).
44. Li, J. et al. A fundamental viewpoint on the hydrogen spillover phenomenon of electrocatalytic hydrogen evolution. *Nat. Commun.* **12**, 3502 (2021).
45. Dang, Y. et al. Partially reduced Ru/RuO₂ composites as efficient and pH-universal electrocatalysts for hydrogen evolution. *Energy Environ. Sci.* **14**, 5433–5443 (2021).
46. Cai, C. et al. Optimizing hydrogen binding on Ru sites with RuCo alloy nanosheets for efficient alkaline hydrogen evolution. *Angew. Chem. Int. Ed.* **61**, e202113664 (2022).
47. Mao, J. J. et al. Isolated Ni atoms dispersed on Ru nanosheets: high-performance electrocatalysts toward hydrogen oxidation reaction. *Nano Lett.* **20**, 3442–3448 (2020).
48. Della Longa, S., Arcovito, A., Girasole, M., Hazemann, J. & Benfatto, M. Quantitative analysis of X-ray absorption near edge structure data by a full multiple scattering procedure: The Fe-CO geometry in photolyzed carbonmonoxy-myoglobin single crystal. *Phys. Rev. Lett.* **87**, 155501 (2001).
49. Wu, Z. et al. Sulfur K-edge X-ray-absorption study of the charge transfer upon lithium intercalation into titanium disulfide. *Phys. Rev. Lett.* **77**, 2101–2104 (1996).
50. Kresse, G. & Furthmüller, J. Efficient iterative schemes for ab initio total-energy calculations using a plane-wave basis set. *Phys. Rev. B* **54**, 11169–11186 (1996).
51. Perdew, J. P., Burke, K. & Ernzerhof, M. Generalized gradient approximation made simple. *Phys. Rev. Lett.* **77**, 3865–3868 (1996).
52. Grimme, S. Semiempirical GGA-type density functional constructed with a long-range dispersion correction. *J. Comput. Chem.* **27**, 1787–1799 (2006).
53. Nørskov, J. K. et al. Origin of the overpotential for oxygen reduction at a fuel-cell cathode. *J. Phys. Chem. B* **108**, 17886–17892 (2004).
54. Atkins, P., De Paula, J., Keeler, J. *Atkins' Physical Chemistry* (Oxford University Press, 2017).

Acknowledgements

This work was financially supported by the National Natural Science Foundation of China (No. 52171224). B.X.Z. acknowledges support from China Postdoctoral Science Foundation (No. 2021M692757) and the National Postdoctoral Program for Innovative Talents (No. BX2021251). The authors thank the staff of beamline BL11B at the Shanghai

Synchrotron Radiation Facility and the staff at Photoemission End-station (BL10B) in the National Synchrotron Radiation Laboratory (NSRL) for their support in XAFS measurements.

Author contributions

B.X.Z. performed the whole experiments. B.H.Z., G.Q.Z., J.M.W. D.Q.L., and Y.P.C. helped in electrocatalysis experiments and material characterizations. L.X.X. helped in DFT calculations. H.G.P., M.X.G., Y.F.L, W.P.S., and B.X.Z. analyzed the data. All the authors contributed to the overall scientific discussions and edited the manuscript. W.P.S., H.G.P., and B.X.Z. conceived the idea and co-wrote the paper.

Competing interests

The authors declare no competing interests.

Additional information

Supplementary information The online version contains supplementary material available at <https://doi.org/10.1038/s41467-022-33625-x>.

Correspondence and requests for materials should be addressed to Wenping Sun or Hongge Pan.

Peer review information *Nature Communications* thanks Elena

Davydova and the other anonymous reviewer(s) for their contribution to the peer review of this work. Peer review reports are available

Reprints and permission information is available at <http://www.nature.com/reprints>

Publisher's note Springer Nature remains neutral with regard to jurisdictional claims in published maps and institutional affiliations.

Open Access This article is licensed under a Creative Commons Attribution 4.0 International License, which permits use, sharing, adaptation, distribution and reproduction in any medium or format, as long as you give appropriate credit to the original author(s) and the source, provide a link to the Creative Commons license, and indicate if changes were made. The images or other third party material in this article are included in the article's Creative Commons license, unless indicated otherwise in a credit line to the material. If material is not included in the article's Creative Commons license and your intended use is not permitted by statutory regulation or exceeds the permitted use, you will need to obtain permission directly from the copyright holder. To view a copy of this license, visit <http://creativecommons.org/licenses/by/4.0/>.

© The Author(s) 2022